ARTI: An Adaptive Radio Tomographic Imaging System

Ossi Kaltiokallio, Riku Jäntti *Senior Member, IEEE* and Neal Patwari *Member, IEEE*

***Abstract*—Radio tomographic imaging systems use received signal strength measurements between static wireless sensors to image the changes in the radio propagation environment in the area of the sensors, which can be used to localize a person causing the change. To date, spatial models used for such systems are set a priori and do not change. Imaging and tracking performance suffers because of the mismatch between the model and the measurements. Collecting labelled training data requires intensive effort, and the data degrades quickly as the environment changes. This paper provides a means for a radio tomographic imaging system to bootstrap to improve its spatial models using unlabelled data, iteratively improving itself over time. A collection of tracking filters are presented to improve the accuracy of image and coordinate estimates. This paper presents an online method to use these estimates to instantaneously update spatial model parameters. Further, a smoothing method is presented to fine-tune the model with a given finite latency. The development efforts are evaluated using simulations and validated with real-world experiments conducted in three different environments. With respect to another state-of-the-art radio tomographic imaging system, the results suggest that the presented system increases the median tracking accuracy by twofold in the most challenging environment and by threefold when the model parameters are trained using the smoothing method.**

I. Introduction

In received signal strength (RSS)-based device-free localization (DFL) systems, a wireless network is deployed in an area to be monitored. Each device in the network broadcasts packets and stores the RSS received from the other devices in the network. When people are located or move in the environment, they modify the way radio signals propagate, which is observed in the RSS measurements of the sensors in ways that can be used to locate and monitor them [1]. Since, in this type of system, the only source of information is the RSS provided by the radio module of the nodes, the transceivers are commonly referred to as sensors, and the network as a radio frequency (RF) sensor network [2]. As an example, such systems have been exploited for residential monitoring [3], ambient assisted living [4], and military purposes [5]. Accurate localization is dependent on an accurate model for RSS measurements. However, the way in which RSS is a function of the locations of people is highly variable, dependent on the environment, the frequency channel, and the way in which multipath waves interact with the environment and the people within it [2], [6], [7], [8], [4], [9].

There are two widely used approaches to model RSS and to perform localization: fingerprinting [10], [11], [12], and model-based approaches [13], [14], [15], [16]. Fingerprinting methods require a database of training data labelled with a person's location, as the person moves to each possible location in the area. During runtime, the current set of RSS measurements are compared to those in the database to estimate the current location. Instead of location-labelled training data, model-based approaches use an a priori spatial statistical model for the changes in RSS with respect to the locations of the sensors and person. Localization is typically performed via imaging [13], [14] or sequential Monte Carlo [16], [17] methods. With sufficient labelled training data, fingerprinting methods are able to achieve high accuracy, although performance degrades exponentially as the environment is altered [12]. Model-based approaches can be deployed quickly, but the mismatch between the a priori model and the actual RSS changes observed as a function of location results in degraded performance. The paper focuses on model-based approaches and we refer to them as RF tomography systems.

In this paper, we present Adaptive Radio Tomographic Imaging (ARTI), a model-based approach which bootstraps to improve its model over time. There is a chicken-and-egg problem in adapting link RSS models: location estimates using generic a priori models are variable and inaccurate, yet finding an accurate model for any particular link requires accurate location estimates as labels for RSS data. ARTI solves this problem by applying a combination of 1) filtering for the RF tomographic imaging and tracking estimates, 2) RSS modeling, and 3) new online and batch-processing algorithms to adjust model parameters. The result is that ARTI overcomes the need for location-labelled training data and is capable of providing extremely accurate localization.

ARTI operates as illustrated in Fig. 1. In short, the system acquires RSS measurements $\tilde{\mathbf{r}}$ from S sensors of the wireless network and weights the measurements in the *adaptive measurement unit*. The weighted and mean-removed RSS measurements $\mathbf{y}$ are inputted to the *RTI unit* to form a discretized propagation field image $\mathbf{z}^i$ of the monitored area. Thereafter, $\mathbf{z}^i$ are filtered and the person's position $\mathbf{z}^t$ is estimated from the filtered images $\mathbf{x}^i$. A Kalman filter is used to track evolution of the target's state $\mathbf{x}^t$ which is used by the *online estimator unit* to recursively estimate the reference RSS value $\boldsymbol{\mu}$ and expected direction of RSS change $\mathbf{w}$. The *smoothing/batch-training unit* calculates smoothed estimates of $\mathbf{x}^i$ and $\mathbf{x}^t$ which are then used by a batch-training algorithm to estimate parameters of the system.

Ossi Kaltiokallio and Riku Jäntti are with the Department of Communications and Networking, Aalto University, School of Electrical Engineering, Espoo, Finland (email:{name.surname}@aalto.fi).

Neal Patwari is with University of Utah, Department of Electrical and Computer Engineering. email: npatwari@ece.utah.edu

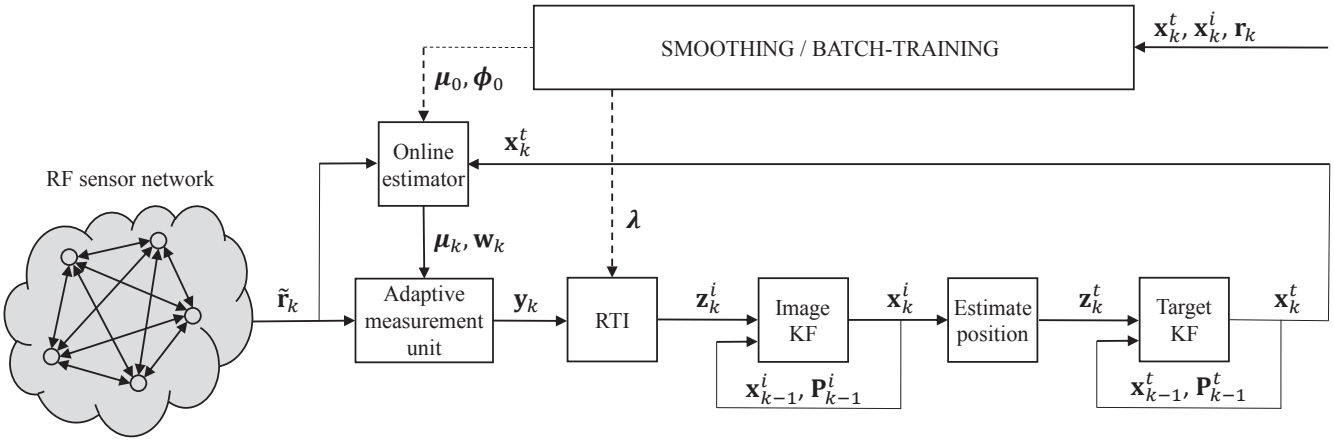

Fig. 1: System overview of ARTI

TABLE I: Major notations

Parameter	Description
$\tilde{r}_{l,c}(k)$	RSS of link l on channel c at time k
$\mu_{l,c}$ and $w_{l,c}$	Reference RSS and weight of measurement system
$\mathbf{y}_k$	Input measurement vector to RTI at time k
$\mathbf{z}_k^i$ and $\mathbf{z}_k^t$	Image and location measurement
$\mathbf{x}_k^i$ and $\mathbf{x}_k^t$	Estimate of image and target states
$\phi_{l,c}$ and $\lambda_{l,c}$	Parameters of RSS model for link l and channel c
$\mathbf{F}$ and $\mathbf{H}$	Transition and measurement matrix
$\mathbf{Q}$ and $\mathbf{V}$	Process and measurement noise

The rest of the paper is organized as follows. In the following section, the related work is discussed. Thereafter, the required background information is introduced and motivation for the work is presented. In Section IV, the components of ARTI are presented. In Section V, the conducted experiments are presented, experimental findings are discussed and the system performance is evaluated using simulations. In Section VI, the development efforts are validated using data from three different environments and thereafter, conclusions are drawn. In Table I, major notations of the paper are summarized.

II. Related Work

RF tomography systems commonly localize the person using an imaging approach referred to as radio tomographic imaging (RTI) [13], [14] or with a Bayesian inference approach which is typically solved using sequential Monte Carlo methods (SMC) [17], [7]. The benefit of RTI is that it is computationally efficient, it provides a global solution and the used spatial model only requires information regarding the size of the elliptic region where the person influences the RSS, which we call the sensitivity region. As a drawback, the temporal RSS changes are not accounted for in the tracking algorithm and information can be lost in the two-step process to first estimate the image and then the location. The benefit of SMC is that the temporal evolution of the measurements are directly related to the kinematic state of the person. However, SMC is computationally more demanding, it only gives a local solution that can converge to a wrong trajectory and it requires a more detailed spatial model to relate the RSS measurements to person's kinematic state, geometry and electrical properties. In this paper, we develop an image filter for RTI that is used to track evolution of the propagation field. In this way, information how the person altered the propagation field at the previous time instant can be included to the tracking algorithm. Also, smoothing filters are presented so that the entire time horizon can be taken into account when estimating unknown states of the system.

Imaging based approaches typically rely on a Kalman filter to track evolution of the target state, that is, coordinates and velocity of the person [9], [18], [19], [20], [21]. In this paper, a Kalman filter is also used to track the image state. This improves the quality of noisy images, it enables to control the delay in image estimates and well known smoothing filters can be used to enhance the images even further. Imaging systems that use RSS variance [18], [21], kernel distance methods that use short- and long-term RSS histograms [19], [20], and channel diversity methods that average the RSS across the set of used channels [8], [9] all introduce a significant delay in the images because the measurements are based on a window of RSS samples. Using RTI and the image filter, the system can be designed so that the delay in the images is smaller than with the aforementioned methods.

The used spatial model relates RSS measurements to the person's location, geometry and electrical properties and it dictates the performance of RF tomography systems. RTI uses a very simplistic model that only requires knowledge about the size of the sensitivity region [13]. On the other hand, SMC methods typically rely on more detailed empirical models such as the exponential [17], magnitude [22] or exponential-Rayleigh [23] models. Theoretical models have also been developed based on diffraction theory [15], [16] and single-bounce reflections [24]. If the model parameters are properly tuned and in line-of-sight (LoS) conditions, it has been shown that SMC methods outperform RTI [17] and the more detailed the model is, the higher the tracking accuracy is [24], [23], [16]. However, many of the aforementioned models have been derived and validated only in LoS conditions and exploiting

them in challenging environments is difficult. The reason being, as the person obstructs the imaginary line connecting the TX-RX pair, which we call the link line, the RSS can increase or remain unchanged rather than decrease [8], [4], [9]. In addition, the sensitivity region is unique for different links [9]. These two empirical findings contradict with the models presented in literature because they commonly assume: i) a decrease in RSS is observed when the link line is obstructed; ii) the parameter that tunes size of the sensitivity region is assumed constant. To overcome this limitation, we extend the exponential model in the context of RTI by estimating the magnitude and direction of RSS change online and use batch-training to fine-tune parameters of the model. This approach is shown to be extremely effective, enabling high accuracy tracking in very difficult environments.

In order for RF sensor networks to function, they require access to calibration data, i.e., RSS measurements that are not altered by the presence of a person. Typically, measurements are gathered during a vacant period and mean of the calibration data is used as the reference RSS value during operation[1]. However, it is not always possible to collect such calibration data, and the reference value can also change over time [3], [4], [25], [19]. In related literature, an exponentially weighted moving average (EWMA) has been used to update the reference value and to make the system adaptive [3], [7], [19]. The drawback of using EWMA is that if the person remains stationary for a long time period, the EWMA will slowly converge to the current value and the person will blend in to the noise of the estimated images making localization impossible [3], [19]. This issue has been addressed by only updating the reference RSS for links that are far away from the person [4] or by identifying the links that are not altered by the person [7], [25]. We expand the work in [4] by developing a logic that makes the decision about parameter update. If the conditions are satisfied, the reference RSS is estimated online using EWMA and only links that are far away from the estimated position are updated. On the other hand, when the person is close to the link line, the magnitude of RSS change is estimated using EWMA and based on the value, the used measurement model is updated.

III. Background

A. Preliminaries

We consider scenarios where S wireless sensors are deployed in the monitored area. Each sensor broadcasts and receives packets from other sensor of the network. The sensors form L unique links that are programmed to communicate over C channels. A link is represented with a 2-tuple (l, c) where l is the link and c the channel identifier. The monitored area is discretized using a grid of N voxels. The position of voxel n is denoted as $\mathbf{p}_n = [x_n \quad y_n]^T$ where x_n and y_n are coordinates of the voxel. Correspondingly, the coordinates of TX and RX of link l are denoted as $\mathbf{p}_l^{tx}$ and $\mathbf{p}_l^{rx}$ in corresponding order.

[1]The reference value is not always the mean. For example, [7] uses a Gaussian distribution and [19] uses a long-term RSS histogram to describe the reference RSS measurements.

The sensors communicate in TDMA fashion and the transmission sequence is based on the sensors' built-in ID numbers. One TDMA cycle consists of S transmissions, one from each sensor. After the cycle, the sensors switch synchronously to the next frequency channel found in a list predefined by the user and a new TDMA cycle is started. The TDMA cycles are sequential, and a transmission from each sensor on each channel forms a communication round consisting of $S \cdot C$ transmissions. After the communication round, the sensors switch to the first frequency channel on the list and a new communication round is started.

B. Radio Tomographic Imaging

The objective of RTI is to estimate changes in the propagation field of the monitored area and to locate the person causing the change. This objective is fulfilled by monitoring the changes in RSS and forming a discretized propagation field image using a projection matrix.

The mean-removed RSS measurements for link l on channel c can be expressed as

$$r_{l,c}(k) = \tilde{r}_{l,c}(k) - \mu_{l,c}(k). \tag{1}$$

where $\tilde{r}_{l,c}(k)$ is the measured RSS and $\mu_{l,c}(k)$ the reference RSS value. In the discretized RTI model, it is assumed that $r_{l,c}(k)$ is a linear combination of the changes in each voxel plus noise [14]

$$r_{l,c}(k) = \sum_{n=1}^{N} [a_{l,n} \cdot b_{n,c}(k)] + \eta_{l,c}(k), \tag{2}$$

where $b_{n,c}$ is the RSS change in voxel n on channel c, $a_{l,n}$ the weight of voxel n for link l, N the number of voxels and $\eta_{l,c}(k)$ the measurement noise. The weighting how each voxel n impacts the RSS change of each link l is described by a geometrical ellipse model

$$a_{l,n} = d_l^{-1/2} \cdot e^{-\Delta_{l,n}/\lambda}, \tag{3}$$

where $d_l = \|\mathbf{p}_l^{tx} - \mathbf{p}_l^{rx}\|$ is the link length and $\|\cdot\|$ denotes the Euclidean norm, $\Delta_{l,n} = \|\mathbf{p}_l^{tx} - \mathbf{p}_n\| + \|\mathbf{p}_l^{rx} - \mathbf{p}_n\| - d_l$ is excess path length of voxel n with respect to link l and λ is decay rate of the model defining sensitivity region of the link. Various weighting models have been proposed in the literature and the readers are referred to [26], [27] and the references therein for details about other weighting options.

RTI systems that exploit channel diversity weight the channel measurements using

$$y_{l,c}(k) = w_{l,c}(k) \cdot r_{l,c}(k), \tag{4}$$

where $w_{l,c}(k)$ is a scalar weight[2]. When all links of the RF sensor network are considered, the changes in the propagation field can be modeled as

$$\mathbf{y}_c(k) = \mathbf{A}\mathbf{b}_c(k) + \boldsymbol{\eta}_c(k), \tag{5}$$

where $\mathbf{y}_c \in \mathbb{R}^{L\times 1}$ and $\boldsymbol{\eta}_c \in \mathbb{R}^{L\times 1}$ are the weighted measurements and noise of the L links, $\mathbf{b}_c \in \mathbb{R}^{N\times 1}$ is the

[2]Typically, RTI systems reduce a link's multi-channel RSS measurements to a scalar value by weighting and averaging, i.e., $y_l(k) = \frac{1}{C}\sum_{c=1}^{C} w_{l,c}(k) \cdot r_{l,c}(k)$ [8], [3], [4].

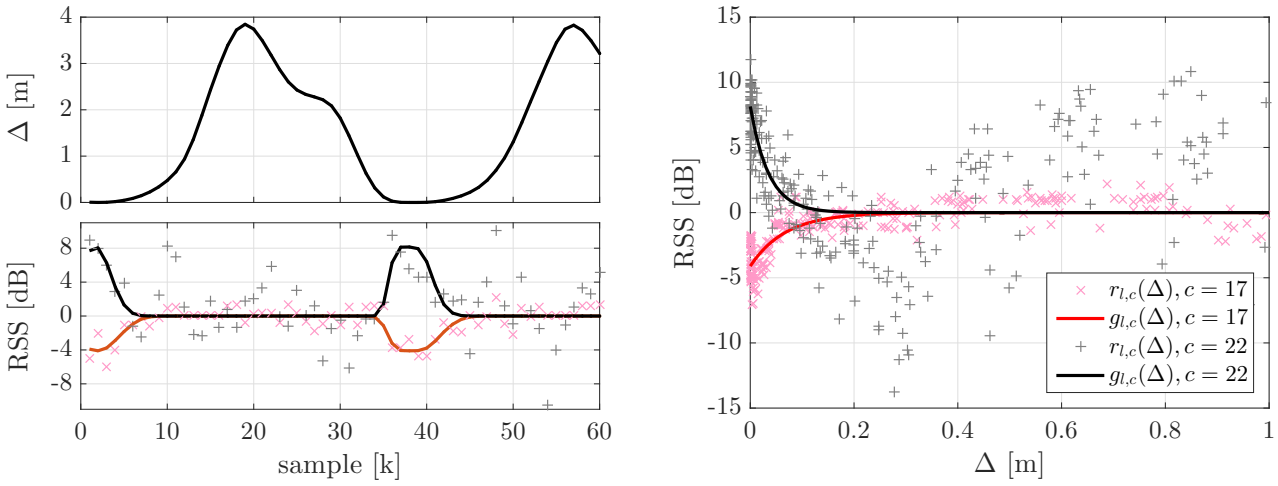

(a) RSS vs. time

(b) RSS vs. Δ

Fig. 2: $r_{l,c}(k)$ and $g_{l,c}(k;\boldsymbol{\theta}_{l,c})$ as a function of time in (a) and as a function of Δ in (b)

radio tomographic image to be estimated, and $\mathbf{A} \in \mathbb{R}^{L\times N}$ is the weight matrix where each column represents a single voxel of the image and each row the weight of each voxel for that particular link. Estimating the image vector $\mathbf{b}_c$ given $\mathbf{y}_c$ is an ill-posed inverse problem and a regularized least-squares estimator is given by [28]

$$\begin{aligned} \mathbf{z}^i(k) &= \mathbf{\Pi}\mathbf{y}_c(k), \\ \mathbf{\Pi} &= \left(\mathbf{A}^T\mathbf{A} + \gamma\mathbf{C}^{-1}\right)^{-1}\mathbf{A}^T, \end{aligned} \tag{6}$$

where γ is a regularization parameter which can be tuned to emphasize either the prior on the image covariance or the measurement. The elements of covariance matrix $\mathbf{C}$ are calculated using an exponential spatial decay [28]

$$\{\mathbf{C}\}_{m,n} = e^{-\|\mathbf{p}_m - \mathbf{p}_n\|/\delta}, \tag{7}$$

where δ is the correlation distance, and m and n denote the voxel indexes. Alternative regularization methods are possible [29] and improved linear estimators can be developed when better noise models are available [21].

From the estimated image $\mathbf{z}^i(k) \in \mathbb{R}^{N\times 1}$, a person can be localized by finding voxel n with highest intensity

$$\mathbf{z}^t(k) = [x_n \quad y_n]^T, \quad \text{where} \quad n = \arg\max\ \mathbf{z}^i(k). \tag{8}$$

In this paper, we only consider localizing a single person. Multiple target tracking is not within the scope of this paper, and the readers are referred to [30], [31] and the references therein for further details. However, we wish to point out that ARTI enhances the accuracy of the images and it would also increase the performance of RTI systems that are capable of localizing more than one person.

C. Motivation

In related literature, the mean-removed RSS measurements are commonly modeled using an exponential model [17]

$$\begin{aligned} g_{l,c}(k;\boldsymbol{\theta}_{l,c}) &= \mathbb{E}[r_{l,c}(k)] \\ g_{l,c}(k;\boldsymbol{\theta}_{l,c}) &\triangleq \phi_{l,c}\cdot e^{-\Delta_l(k)/\lambda_{l,c}}, \end{aligned} \tag{9}$$

where $\boldsymbol{\theta}_{l,c} = \begin{bmatrix}\phi_{l,c} & \lambda_{l,c}\end{bmatrix}$ are parameters of the model for which $\phi_{l,c}$ defines the magnitude and direction of RSS change when the person is on the link line and $\lambda_{l,c}$ is a parameter that controls the decay rate with respect to excess path length $\Delta_l(k)$. As an example, $r_{l,c}$ and $g_{l,c}$ for two different channels of the same link are illustrated as a function of time in Fig. 2a and as a function of Δ in Fig. 2b. For channel 17, $\phi = -4.106$ and $\lambda = 0.068$ whereas for channel 22, $\phi = 8.147$ and $\lambda = 0.035$. Since the model parameters differ between links and channels, using fixed values for them limits the achievable accuracy of RF tomography systems. To overcome this limitation, we develop an online estimator for $\phi_{l,c}$ in this paper and update the weigthing in Eq. (4) correspondingly. Moreover, batch-training is used to fine-tune the estimates of $\phi_{l,c}$ and $\lambda_{l,c}$ which can then be used in the future.

IV. Methodology

A. Linear State Space Models

To define the problem of tracking, consider evolution of the state sequence given by

$$\mathbf{x}_k = \mathbf{F}\mathbf{x}_{k-1} + \mathbf{q}_{k-1}, \tag{10}$$

where $\mathbf{x}_k$ is state of the system at time step k, $\mathbf{F}$ the transition matrix describing dynamics of the system and $\mathbf{q}_{k-1} \sim \mathcal{N}(\mathbf{0}, \mathbf{Q}_{k-1})$ the process noise. The objective of tracking it to recursively estimate $\mathbf{x}_k$ from measurements

$$\mathbf{z}_k = \mathbf{H}\mathbf{x}_k + \mathbf{v}_k, \tag{11}$$

where $\mathbf{H}$ is the measurement model matrix and $\mathbf{v}_k \sim \mathcal{N}(\mathbf{0}, \mathbf{V}_k)$ the measurement noise.

In this paper, we track both the state of the voxels and target. The voxel state is composed of voxel intensity and its derivative. The target state is composed of the person's location and velocity. Such systems can be modeled using a

Algorithm 1: ARTI algorithm

for $k = 1 : K$ — *At time instant k*
- $\mathbf{z}_k^i = \mathbf{\Pi}\mathbf{y}_k$, where $\mathbf{y}_k = \mathbf{w}_c \circ [\tilde{\mathbf{r}}_c(k) - \boldsymbol{\mu}_c]$ — *Form meas. and compute image using* (6)
- $[\mathbf{x}_k^i,\ \mathbf{P}_k^i] = \text{kalmanfilter}(\mathbf{x}_{k-1}^i,\ \mathbf{P}_{k-1}^i,\ \mathbf{z}_k^i)$ — *Estimate image state with* (17) *and* (18)
- $\mathbf{z}_k^t = [x_n \quad y_n]^T$, where $n = \arg\max\ \mathbf{H}^i\mathbf{x}_k^i$ — *Estimate position from filtered image*
- $[\mathbf{x}_k^t,\ \mathbf{P}_k^t] = \text{kalmanfilter}(\mathbf{x}_{k-1}^t,\ \mathbf{P}_{k-1}^t,\ \mathbf{z}_k^t)$ — *Estimate target state with* (17) *and* (18)
- **if** $\|\mathbf{z}_k^t - \mathbf{H}^t\mathbf{F}^t\mathbf{x}_{k-1}^t\| < T_n$ and $\|[\dot{x}_k^t \quad \dot{y}_k^t]\| > T_s$ — *Condition meas. residual and speed on thresholds*
  - $[\boldsymbol{\phi}_c,\ \boldsymbol{\mu}_c,\ \boldsymbol{w}_c] = \text{estimator}(\boldsymbol{\phi}_c,\ \boldsymbol{\mu}_c,\ [x_k^t \quad y_k^t]^T)$ — *Update reference RSS and weight used in* (1) *and* (4)
- **end**

end

Algorithm 2: $[\boldsymbol{\phi}_c,\ \boldsymbol{\mu}_c,\ \boldsymbol{w}_c] = \text{estimator}(\boldsymbol{\phi}_c,\ \boldsymbol{\mu}_c,\ \mathbf{p}_k)$

for *l = 1:L* — *For link l*
- $\Delta_l = \|\mathbf{p}_l^{tx} - \mathbf{p}_k\| + \|\mathbf{p}_l^{rx} - \mathbf{p}_k\| - \|\mathbf{p}_l^{tx} - \mathbf{p}_l^{rx}\|$ — *Compute excess path length*
- **if** $\Delta_l \leq 2\lambda$, $\phi_{l,c} = \alpha\phi_{l,c} + (1-\alpha)(\tilde{r}_{l,c}(k) - \mu_{l,c})$, **end** — *Person is close to link line, update $\phi_{l,c}$*
- **if** $\Delta_l > 2\lambda$, $\mu_{l,c} = \alpha\mu_{l,c} + (1-\alpha)\tilde{r}_{l,c}(k)$, **end** — *Person is far away from link line, update $\mu_{l,c}$*
- $w_{l,c} = \text{sgn}\{\phi_{l,c}\}$

end

$\circ$ denotes element-wise vector product, $\|\cdot\|$ the Euclidean norm, $(\cdot)^T$ the transpose and $\text{sgn}\{\cdot\}$ the sign function

discrete white noise acceleration (DWNA) model where the first derivative of the system is perturbed with a zero-mean white acceleration sequence. The transition matrix, process noise and measurement model of a single dimension DWNA model are [32, Ch. 6]

$$\mathbf{F} = \begin{bmatrix} 1 & dt \\ 0 & 1 \end{bmatrix} \quad \mathbf{Q} = \begin{bmatrix} \frac{1}{3}dt^3 & \frac{1}{2}dt^2 \\ \frac{1}{2}dt^2 & dt \end{bmatrix} \quad \mathbf{H} = \begin{bmatrix} 1 \\ 0 \end{bmatrix}^T \tag{12}$$

where dt is the sampling interval.

The image state can be expressed as

$$\mathbf{x}^i = \begin{bmatrix} x_1^i & x_2^i & \dots & x_N^i \\ \dot{x}_1^i & \dot{x}_2^i & \dots & \dot{x}_N^i \end{bmatrix}, \tag{13}$$

where x_j^i denotes intensity and $\dot{x}_j^i$ intensity change rate of voxel j. The transition matrix, measurement model, and noise processes of the imaging system are

$$\mathbf{F}^i = \mathbf{F}, \quad \mathbf{Q}^i = q^i\mathbf{Q}, \quad \mathbf{H}^i = \mathbf{H}, \quad \mathbf{V}^i = v^i. \tag{14}$$

Respectively, the target state can be expressed as

$$\mathbf{x}^t = [x^t \quad \dot{x}^t \quad y^t \quad \dot{y}^t]^T, \tag{15}$$

where x^t and y^t denote position and $\dot{x}^t$ and $\dot{y}^t$ velocity of the target in the Cartesian coordinate system. The transition matrix, measurement model, and noise processes of the target system are

$$\begin{aligned} \mathbf{F}^t &= \begin{bmatrix} \mathbf{F} & \mathbf{0}^{2\times2} \\ \mathbf{0}^{2\times2} & \mathbf{F} \end{bmatrix} \quad \mathbf{Q}^t = q^t \begin{bmatrix} \mathbf{Q} & \mathbf{0}^{2\times2} \\ \mathbf{0}^{2\times2} & \mathbf{Q} \end{bmatrix} \\ \mathbf{H}^t &= \begin{bmatrix} \mathbf{H} & \mathbf{0}^{1\times2} \\ \mathbf{0}^{1\times2} & \mathbf{H} \end{bmatrix} \qquad \mathbf{V}^t = \begin{bmatrix} v^t & 0 \\ 0 & v^t \end{bmatrix}. \end{aligned} \tag{16}$$

B. Kalman Filter

In case $\mathbf{F}$ and $\mathbf{H}$ are linear, time-invariant and the noise sequences $\mathbf{q}_{k-1}$ and $\mathbf{v}_k$ Gaussian, the Kalman filter yields the optimal solution to the tracking problem in the least squares sense. The recursion of the filter can be divided into the prediction stage [32, Ch. 5.2]

$$\begin{aligned} \mathbf{x}_k^- &= \mathbf{F}\mathbf{x}_{k-1} \\ \mathbf{P}_k^- &= \mathbf{F}\mathbf{P}_{k-1}\mathbf{F}^T + \mathbf{Q}. \end{aligned} \tag{17}$$

Thereafter, the state and covariance are updated when measurement $\mathbf{z}_k$ becomes available using the following recursion

$$\begin{aligned} \mathbf{S}_k &= \mathbf{H}\mathbf{P}_k^-\mathbf{H}^T + \mathbf{V} \\ \mathbf{K}_k &= \mathbf{P}_k^-\mathbf{H}^T\mathbf{S}_k^{-1} \\ \mathbf{x}_k &= \mathbf{x}_k^- + \mathbf{K}_k(\mathbf{z}_k - \mathbf{H}\mathbf{x}_k^-) \\ \mathbf{P}_k &= \mathbf{P}_k^- - \mathbf{K}_k\mathbf{S}_k\mathbf{K}_k^T. \end{aligned} \tag{18}$$

The equations to compute covariance $\mathbf{P}_k$ and Kalman gain $\mathbf{K}_k$ are independent of the measurements implying that the sequence could be calculated beforehand and that they converge to a constant, i.e., $\mathbf{P}_k \to \mathbf{P}$ and $\mathbf{K}_k \to \mathbf{K}$. Thus, the N voxels can share the same covariance matrix while having independent states. This allows us to compute the prediction and update stages using matrix multiplies and additions, and the inversion in Eq. (18) is calculated only once. This reduces the computational overhead notably with respect to a solution with N independent filters running in parallel.

In the experiments, the image filter is initialized using the first created image and the change rate is set to zero, i.e., $\mathbf{x}_1^i = \begin{bmatrix} \mathbf{z}_1^i & \mathbf{0}^{N\times1} \end{bmatrix}^T$. The covariance is initialized as $\mathbf{P}_1^i = \mathbf{I}^{2\times2}$, where $\mathbf{I}$ is a unit matrix. Correspondingly, the target state is initialized using the position estimate of the first image given by Eq. (8) and velocity is set to zero, i.e., $\mathbf{x}_1^t = \begin{bmatrix} x_j & 0 & y_j & 0 \end{bmatrix}^T$ with covariance $\mathbf{P}_1^t = \mathbf{I}^{4\times4}$.

C. Online Estimator

It is well known that the steady-state channel characteristics change in time if the surrounding environment is altered [1], [7], [25]. In long-term deployments and in domestic environments this is inevitable as doors and windows can be opened or closed, daily commodities are consumed and moved, and furniture might be relocated or replaced [3], [4], [12]. Under such conditions, it is mandatory to estimate the reference RSS $\mu_{l,c}$ online. We have also identified that if $\phi_{l,c}$ used in Eq (9) is known for each channel and link, it significantly improves the system performance. Since the model defined in Eq. (3) only requires knowledge about size of the sensitivity region, we do not need to know the exact

value of $\phi_{l,c}$, it is sufficient to know the expected direction of RSS change when the person obstructs the link line. Thus, we estimate $\phi_{l,c}$ online and set the weight used in Eq. (4) as $w_{l,c} \triangleq \text{sgn}\{\phi_{l,c}\}$, where $\text{sgn}\{\cdot\}$ denotes the sign function. The pseudocode of ARTI is presented in Algorithm 1 and the online estimator for $\mu_{l,c}$ and $\phi_{l,c}$ in Algorithm 2.

The logic to update $\mu_{l,c}$ and $\phi_{l,c}$ is straightforward. First, we compute the measurement residual $\|\mathbf{z}_k^t - \mathbf{H}^t\mathbf{F}^t\mathbf{x}_{k-1}^t\|$ and only update the parameters if the current position measurement is inline with the kinematic model estimate. Small residual values indicate that the state estimate can be trusted. Second, the parameters are updated only when the target is moving. If the person is stationary, the current location estimate can be inaccurate which would lead to incorrect estimates of $\mu_{l,c}$ and $\phi_{l,c}$. In this case, the future location estimates would also contain this error. If the two conditions hold, $\mu_{l,c}$ is updated when the person is far away from the link line ($\Delta_l > 2\lambda$). Otherwise, $\phi_{l,c}$ is updated to capture the expected direction of RSS change when the person is near the link line ($\Delta_l \leq 2\lambda$).

In the experiments, the reference RSS is initialized using $\mu_{l,c}(0) = \frac{1}{T+1}\sum_{k=-T}^{0}\tilde{r}_{l,c}(k)$, where $\tilde{r}_{l,c}(k)$ are gathered during an initial training period when the monitored area is vacant. In Section VI-D, we discuss the scenario where $\mu_{l,c}$ is initialized without a training period. The weight used in Eq. (4) is initialized as $w_{l,c}(0) = \text{sgn}\{\phi_0\}$ and $\phi_0 = -1e^{-3}$. The initial value of ϕ_0 is selected negative because it is more likely that attenuation is measured when the person obstructs the link line (see Section V-B and Table III) and a value close to zero is used so that the estimate changes its sign rapidly if $\phi_{l,c} > 0$.

D. Smoothing Filters

Sometimes, it is of interest to estimate states of the system for each time instant k conditioned on all the measurements up to time step K, where $K > k$. This problem can be solved with Bayesian smoothing, which in general, improves the state estimates and decreases the covariance. One Bayesian smoother is the discrete-time Kalman smoother, also known as the Rauch-Tung-Striebel smoother (RTSS) and it can be used for computing smoothed estimates of the model given in Eq. (10). The smoothed state estimate $\tilde{\mathbf{x}}_k$ and covariance $\tilde{\mathbf{P}}_k$ can be calculated with the following recursion [33, Ch. 8]

$$\begin{aligned}\mathbf{P}_{k+1}^{-} &= \mathbf{F}\mathbf{P}_k\mathbf{F}^T + \mathbf{Q}\\ \mathbf{G}_k &= \mathbf{P}_k\mathbf{F}^T(\mathbf{P}_{k+1}^{-})^{-1}\\ \tilde{\mathbf{x}}_k &= \mathbf{x}_k + \mathbf{G}_k(\tilde{\mathbf{x}}_{k+1} - \mathbf{F}\mathbf{x}_k)\\ \tilde{\mathbf{P}}_k &= \mathbf{P}_k + \mathbf{G}_k(\tilde{\mathbf{P}}_{k+1} - \mathbf{P}_{k+1}^{-})\mathbf{G}_k^T,\end{aligned} \tag{19}$$

where $\mathbf{x}_k$ and $\mathbf{P}_k$ are the Kalman filter estimates for the mean and covariance, and $\mathbf{G}_k$ is the smoother gain at time step k. The difference between the Kalman filter and RTSS is that the recursion in the filter moves forward whereas in the smoother backwards. In the smoother, recursion starts from the last time step K with initial estimates $\tilde{\mathbf{x}}_K = \mathbf{x}_K$ and $\tilde{\mathbf{P}}_K = \mathbf{P}_K$.

Another possibility for smoothing is to use a two filter based smoother (TFS) in which a Kalman filter is used in the forward recursion and an information filter is used in the backward recursion [34]. The prediction step of the information filter is given by

$$\begin{aligned}\mathbf{K}_k^b &= \mathbf{M}_{k+1}^b\left(\mathbf{M}_{k+1}^b + \mathbf{Q}^{-1}\right)^{-1}\\ \mathbf{m}_k^{-} &= \mathbf{F}^T\left(\mathbf{I} - \mathbf{K}_k^b\right)\mathbf{m}_{k+1}^b\\ \mathbf{M}_k^{-} &= \mathbf{F}^T\left(\mathbf{I} - \mathbf{K}_k^b\right)\mathbf{M}_{k+1}^b\mathbf{F},\end{aligned} \tag{20}$$

where $\mathbf{I}$ is the identity matrix. The information vector $\mathbf{m}_k^b$ and information matrix $\mathbf{M}_k^b$ are updated using

$$\begin{aligned}\mathbf{m}_k^b &= \mathbf{m}_k^{-} + \mathbf{H}^T\mathbf{R}^{-1}\mathbf{z}_k\\ \mathbf{M}_k^b &= \mathbf{M}_k^{-} + \mathbf{H}^T\mathbf{R}^{-1}\mathbf{H}.\end{aligned} \tag{21}$$

The smoothed state estimate $\tilde{\mathbf{x}}_k$ and covariance $\tilde{\mathbf{P}}_k$ is a combination of the forward and backward filter outputs

$$\begin{aligned}\mathbf{G}_k &= \mathbf{P}_k\mathbf{M}_k^{-}\left(\mathbf{I} + \mathbf{P}_k\mathbf{M}_k^{-}\right)^{-1}\\ \tilde{\mathbf{P}}_k &= \left((\mathbf{P}_k)^{-1} - \mathbf{M}_k^{-}\right)^{-1}\\ \tilde{\mathbf{x}}_k &= \left(\mathbf{I} - \mathbf{G}_k\right)\mathbf{x}_k + \tilde{\mathbf{P}}_k\mathbf{m}_k^{-},\end{aligned} \tag{22}$$

where $\mathbf{x}_k$ and $\mathbf{P}_k$ are the Kalman filter estimates for the mean and covariance and $\mathbf{m}_k^{-}$ and $\mathbf{M}_k^{-}$ are the predicted information vector and information matrix. As in RTSS, recursion starts from the last time step K with initial estimates $\tilde{\mathbf{x}}_K = \mathbf{x}_K$ and $\tilde{\mathbf{P}}_K = \mathbf{P}_K$.

In this paper, three different algorithms for smoothing the state estimates are considered and they are presented in the following. The algorithms output smoothed estimates of the target state $\tilde{\mathbf{x}}_k^t$ and covariance $\tilde{\mathbf{P}}_k^t$.

1) RTSS-target (RTSS-T): The state estimates of the tracked target are smoothed using RTSS. The state space models are given in Eqs. (15) and (16) and the state estimate and covariance used in Eq. (19) are $\mathbf{x}_k = \mathbf{x}_k^t$ and $\mathbf{P}_k = \mathbf{P}_k^t$.

2) RTSS-image and target (RTSS-IT): The estimated images are smoothed using RTSS. The state space models are given in Eqs. (13) and (14) and the state estimate and covariance used in Eq. (19) are $\mathbf{x}_k = \mathbf{x}_k^i$ and $\mathbf{P}_k = \mathbf{P}_k^i$. After smoothing the images, new position estimates are calculated from the smoothed images and a Kalman filter is used to track the target state $\mathbf{x}_k^t$ and covariance $\mathbf{P}_k^t$. Thereafter, the target state and covariance are smoothed with RTSS as in the previous algorithm to obtain $\tilde{\mathbf{x}}_k^t$ and $\tilde{\mathbf{P}}_k^t$.

3) TFS-image and target (TFS-IT): The algorithm is the same as presented in Algorithm 1 with three differences. First, the recursion runs backward in time starting from time sample K. Second, the image Kalman filter is replaced by the information filter given in Eqs. (20) and (21) and by the TFS given in Eq. (22). The initial estimates of the information filter are $\mathbf{m}_K^b = \mathbf{0}^{2\times N}$ and $\mathbf{M}_K^b = \mathbf{0}^{2\times 2}$ [34]. Third, the target Kalman filter uses the position estimates calculated from the smoothed images. At the end of the recursion, the state estimates of the tracked target are smoothed using RTSS to obtain $\tilde{\mathbf{x}}_k^t$ and $\tilde{\mathbf{P}}_k^t$. This algorithm differs notably from the other two since $\mu_{l,c}$ and $\phi_{l,c}$ are re-estimated in the backward recursion.

E. Training

Training parameters of the exponential model requires the mean-removed RSS measurements $r_{l,c}(k)$ and excess path

(a) Open environment (Ex. 1)

(b) Apartment deployment (Ex. 2 and 3)

(c) Through-wall scenario (Ex. 4)

Fig. 3: The three experiment environments. Experimental layout of the apartment and through-wall environments are illustrated in Fig. 9

length $\Delta_l(k)$ of the person with respect to link l. Using the smoothed target state estimates $\tilde{\mathbf{x}}_k^t$, $\Delta_l(k)$ with respect to location of the person $\mathbf{p}_k = \mathbf{H}^t\tilde{\mathbf{x}}_k^t$ is calculated as

$$\Delta_l(k) = \|\mathbf{p}_l^{tx} - \mathbf{p}_k\| + \|\mathbf{p}_l^{rx} - \mathbf{p}_k\| - \|\mathbf{p}_l^{tx} - \mathbf{p}_l^{rx}\|. \quad (23)$$

Given $r_{l,c}(k)$ and $\Delta_l(k)$, parameters $\boldsymbol{\theta}_{l,c} = \begin{bmatrix}\phi_{l,c} & \lambda_{l,c}\end{bmatrix}$ of the exponential model can be estimated by minimizing the cost function

$$J(\boldsymbol{\theta}_{l,c}) = \sum_{k=1}^{K} \left[r_{l,c}(k) - g_{l,c}(k;\boldsymbol{\theta}_{l,c})\right]^2, \quad (24)$$

where $g_{l,c}(k;\boldsymbol{\theta}_{l,c})$ is the exponential model defined in Eq. (9). In this paper, we use a Nelder-Mead simplex algorithm [35] to find the minimum of $J(\boldsymbol{\theta}_{l,c})$.

The trained parameters are used when re-initializing the system. In other words, $\phi_{l,c}$ is used as the initial estimate in the online estimator, i.e., $\phi_0 = \phi_{l,c}$ and $w_{l,c}(0) = \text{sgn}\{\phi_0\}$. On the other hand, λ is substituted with $\lambda_{l,c}$ in Eq. (3) to update the weighting for each link, channel and voxel. Thereafter, $\mathbf{\Pi}$ is calculated using Eq. (6) and the projection matrix becomes unique for each frequency channel. As an example, $r_{l,c}$ and $g_{l,c}$ with the trained model parameters is illustrated in Fig. 2. For channel 17, $\phi_{l,c} = -4.106$ and $\lambda_{l,c} = 0.068$ and these values are used for this channel and link when re-initializing the system.

V. Experiments

In this section, the experimental setting and conducted tests are introduced. Thereafter, empirical findings how model parameters ϕ and λ differ between links and environments is presented. At the end of the section, the presented system is numerically evaluated using simulations.

A. Experiment Description

The used wireless sensors are Texas Instruments CC2531 USB dongles, operating at the maximum transmit power ($+4.5$ dBm) [36]. The IEEE 802.15.4 standard [37] specifies 16 channels ($c \in [11, \ldots, 26]$) within the 2.4 GHz ISM band and they are 5 MHz apart, having a 2 MHz bandwidth. The sensors communicate in TDMA fashion on multiple frequency channels as explained in Section III-A. In each packet, the sensors include their ID and the most recent RSS measurements of the packets received from other sensors of the network. If a packet is dropped, the next sensor in the schedule transmits after a backoff time, thus increasing the network's tolerance to packet drops. The communication protocol is explained in further detail in [4].

TABLE II: Experimental Parameters

	Parameter	Value	Description
RTI	p	0.1524	Voxel width [m]
	γ	500	Regularization parameter
	δ	2	Correlation distance [m]
	λ	0.05	Excess path length [m]
ESTIMATOR	α	0.90	Smoothing factor of EWMA
	T_r	1.0	Residual threshold [m]
	T_v	0.2	Velocity threshold [m/s]
FILTERS	q^i	1.0	Process noise of image filter [dB/s^2]
	v^i	0.03	Meas. noise of image filter [dB]
	q^t	2.0	Process noise of target filter [m/s^2]
	v^t	0.5	Meas. noise of target filter [m]

In experiment 1, shown in Fig. 3a, 30 sensors are deployed on the perimeter of an open area (70 m^2). The sensors are placed on podiums at a height of one meter. The sensors are programmed to communicate on channels 11, 17, 22, and 26 so as to cover the entire span of available frequencies. During the test, a person walks at constant speed along a rectangular path and the trajectory is covered twice. Markers are placed inside the monitored area for the test person to follow, while a metronome is used to set a predefined walking pace. In this way, each collected RSS measurement can be associated to the true location of the person.

In experiments 2 and 3, shown in Fig. 3b, 33 sensors are deployed in a single-floor, single-bedroom apartment (58 m^2). Most of the sensors are attached on the walls of the apartment, while a few of them are placed elsewhere, e.g., on the edge of a marble counter in the kitchen or on the side of the refrigerator. The antennas of the sensors are detached from the walls by a few centimeters to enhance the localization accuracy [3]. In experiment 2, the sensors are programmed to communicate on channels 15, 20, 25, and 26 in order to avoid the interference generated by several coexisting Wi-Fi

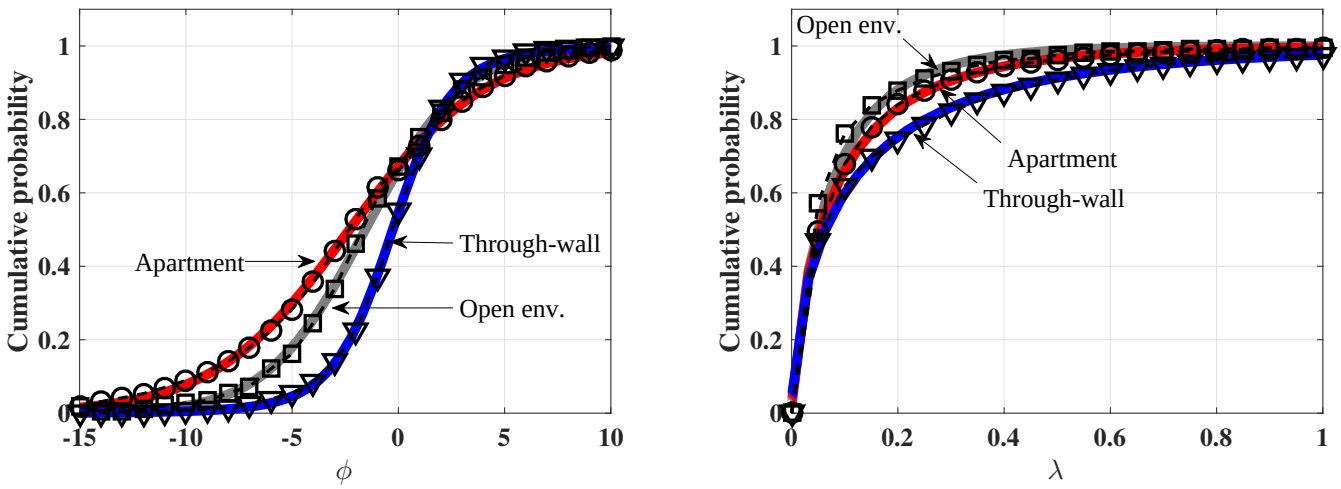

(a) CDF of ϕ (b) CDF of λ

Fig. 4: Empirical CDFs of ϕ and λ in the three environments illustrated with markers and dashed lines. In the figures, fitted models are illustrated with solid color lines.

networks found in the neighboring apartments, which would increase the floor noise level [38]. In experiment 3, the sensors are programmed to communicate on all 16 frequency channels. In both experiments, a person is either standing still at a predefined location or walks from one location to another with constant speed. The trajectory is covered once.

Experiment 4 differs from the other experiments since it is a through-wall experiment as shown in Fig. 3c. In the experiment, 33 sensors are deployed around a lounge room, outside the walls of the room, covering an area of 86 m^2. The sensors are set on podiums at a height of one meter and they are programmed to communicate on all 16 frequency channels. In the experiment, a person walks along a predefined path at constant speed. The path is covered six times.

On average, the time interval between two consecutive transmissions is $dt_k = t_k - t_{k-1} = 2.9$ ms. If $S = 30$ and $C = 4$ as in Ex. 1, one TDMA cycle lasts $dt_c = 30 \cdot dt_k = 87$ ms and one communication round $dt_r = 4 \cdot dt_c = 348$ ms. The image and target filters use $dt = dt_c$. Parameters used in the experiments are given in Table II.

B. Experimental Findings

To get an understanding how parameters ϕ and λ of the exponential model defined in Eq. (9) vary between different links and environments, $g_{l,c}(k; \boldsymbol{\theta}_{l,c})$ is fitted to $r_{l,c}(k)$ using known location of the person. Links that were not intersected by the person during the experiment are omitted from the evaluation. Thereafter, well-known probability distribution are fitted to the empirical distributions to find the best match. The empirical distribution of ϕ closely follows a non-standardized Student's t-distribution $\phi \sim \mathcal{T}(\mu_\phi, \sigma_\phi, \nu_\phi)$ with location parameter μ_ϕ, scale parameter σ_ϕ and shape parameter ν_ϕ. Correspondingly, the empirical distribution of λ closely follows a Weibull distribution $\lambda \sim \mathcal{W}(a_\lambda, b_\lambda)$ with scale parameter a_λ and shape parameter b_λ. The empirical and fitted distributions are shown in Fig. 4 and distribution parameters are given in Table III.

TABLE III: Distribution parameters

	μ_ϕ	σ_ϕ	ν_ϕ	a_λ	b_λ
Open	-1.5537	3.5885	10.0298	0.0772	0.7951
Apartment	-2.2998	4.9506	8.7467	0.0891	0.7076
Through-wall	-0.2644	2.1330	3.9600	0.1158	0.6112

The results are inline with our understanding how the signal strength behaves in various environments. In open environments and when the distance between the transceivers is small, it is expected that the RSS measurements attenuate as the person obstructs the LoS. In the open and apartment environments, μ_ϕ is much smaller than it is in the through-wall experiment. This indicates that it is much more likely that attenuation will be measured in the open and apartment environments when the person is in between the transceivers. In addition, it is more likely in these environments that the person has a larger effect on the link and therefore, σ_ϕ is larger. In the through-wall environment, it is likely that a link is not affected by the person or that the change in RSS is small when the person is close to the link line yielding a small shape parameter σ_ϕ. To note, the sensor distances are on average smaller in the apartment experiment ($\bar{d} = 4.43$ m) than in the open environment ($\bar{d} = 6.28$ m) and there are many links that have LoS communication. Thus, it is understandable why μ_ϕ is smaller and σ_ϕ is larger in the apartment environment.

Size of the spatial region where the person influences the RSS is defined by λ. In the open environment, multipath propagation is not as severe as in the other two environments and the person mainly effects the LoS signal. Thus, λ is small and it does not vary much between the different links. In cluttered environments, multipath propagation is common and the person can also alter the RSS by affecting the multipath

TABLE IV: Median (and 95$^{\text{th}}$ percentile) localization errors in centimeters

		Ex. 1	Ex. 2	Ex. 3	Ex. 4
ONLINE	CDRTI	31.99 (100.19)	18.79 (56.84)	15.74 (69.83)	181.15 (628.35)
	ARTI w/o online est.	31.26 (128.92)	18.47 (64.42)	17.59 (68.05)	200.59 (488.49)
	ARTI	19.82 (47.75)	10.30 (25.40)	10.41 (27.52)	72.91 (378.49)
SMOOTHED	CDRTI, RTSS-T	22.94 (66.13)	15.79 (45.72)	14.78 (62.93)	151.62 (463.70)
	ARTI, RTSS-T	14.33 (36.10)	8.07 (19.30)	6.96 (18.67)	66.02 (256.74)
	ARTI, RTSS-IT	10.09 (31.64)	8.40 (19.26)	6.81 (16.06)	27.69 (279.62)
	ARTI, TFS-IT	7.81 (25.62)	7.82 (17.30)	6.14 (13.18)	13.93 (38.75)

components impinging on the receiver antenna. This increases size of the spatial region where the person influences the link and therefore, λ is larger and deviates more in the apartment and through-wall environments.

C. Numerical Evaluation

In this subsection, the presented system is numerically evaluated using the same sensor positions and trajectories as in the experiments. In the simulations, the RSS measurements are generated using the exponential model given in Eq. (9) and the measurements are corrupted by i.i.d. Gaussian noise, i.e., $\eta_{l,c}(k) \sim \mathcal{N}(0, \sigma_\eta^2)$ where $\sigma_\eta = 2$. Parameters of the exponential model are drawn from $\phi \sim \mathcal{T}(\mu_\phi, \sigma_\phi, \nu_\phi)$ and $\lambda \sim \mathcal{W}(a_\lambda, b_\lambda)$ using the distribution parameters given in Table III and they are assumed i.i.d. for each link and channel. Since no temporal statistical model is known for the changes in RSS over time due to changes in the environment other than people, the reference RSS value is assumed to be constant and known ($\mu_{l,c} = -45$ dB) and it is not updated by Algorithm 2 during simulations. The presented system is evaluated with respect to *channel diversity RTI* (CDRTI) which averages the measurements across the entire set of used channels, i.e., $y_l(k) = -\frac{1}{C}\sum_{c=1}^{C} \tilde{r}_{l,c}(k) - \mu_{l,c}(k)$.

The simulation results are given in Table IV where the median and 95$^{\text{th}}$ percentile localization errors are reported in centimeters for the different experiments. On average, CDRTI achieves comparative accuracy as the presented system w/o online estimation. This is understandable, since the Kalman filter used for enhancing the images essentially acts as a low-pass filter, i.e., averaging the RSS measurements on the different channels (CDRTI) is equivalent to forming the images individually for each channel and then averaging the images together. In this respect, process noise value of the image filter q^i can be viewed as a smoothing parameter. Using a small value ($q^i \ll 1$) corresponds to averaging a large number of successive images together whereas for large values ($q^i > 1$), only the most recent images are taken into account.

With online training enabled, ARTI outperforms CDRTI in every experiment because $w_{l,c}$ is recursively estimated. For CDRTI, an increase in RSS is an indication that a person is not in between the transceivers which is incorrect if $\phi_{l,c} > 0$. For ARTI, the same increase can be informative and indicate the person's location correctly if $w_{l,c} \equiv \text{sgn}\{\phi_{l,c}\}$. Let us group $w_{l,c}$ of links that were intersected during the experiment into a column vector $\hat{\mathbf{w}}$ of size $M \times 1$, where M is the number of crossed links. For these links, we define the true weight as $\tilde{\mathbf{w}}$,

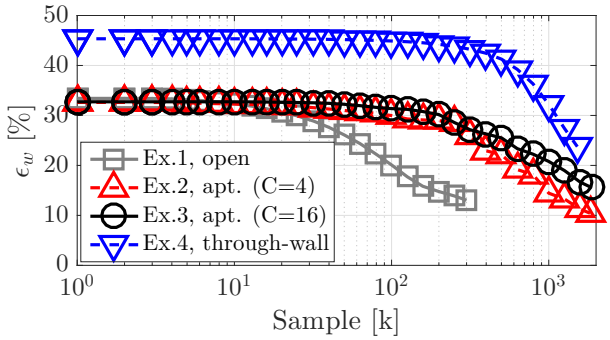

Fig. 5: Error of estimating $w_{l,c}$.

where $\tilde{w}_m = \text{sgn}\{\phi_m\}$ and $\phi_m \sim \mathcal{T}(\mu_\phi, \sigma_\phi, \nu_\phi)$. Now, the percentage error of $\hat{\mathbf{w}}$ can be calculated using

$$\epsilon_w = \frac{100\%}{M} \cdot \sum_{m=1}^{M} \mathbb{1}_m, \quad \mathbb{1}_m = \begin{cases} 1 & \text{if } \tilde{w}_m \neq \hat{w}_m \\ 0 & \text{otherwise} \end{cases} \tag{25}$$

and it is illustrated in Fig. 5 as a function of time for the different experiments. In the open and apartment experiments, the initial estimates is incorrect for approximately 33% of the links whereas in the through-wall experiment for 45% indicating that the through-wall environment is significantly more challenging than the others. The figure also reveals that higher sampling rate of the channel increases the convergence rate of $\hat{\mathbf{w}}$ which is visible by comparing ϵ_w of the apartment experiments. The sampling rate is four times higher in Ex. 2 w.r.t. Ex. 3. In the experiments, the average number of samples the online estimator has to estimate $w_{l,c}$ is $\begin{bmatrix}14.03 & 17.76 & 5.49 & 10.95\end{bmatrix}$ for Ex. $1-4$ in corresponding order. Thus, using channel diversity is a tradeoff between sampling rate and available information. A large number of channels is beneficial for localization purposes because the probability increases that at least one of the channels follows the model. However, the cost of doing so is the lower sampling rate for each channel which inevitably effects performance of the online estimator.

Accuracy of the different smoothing filters are also given in Table IV. In general, smoothing increases the accuracy of the state estimates because the entire time horizon is taken into account. RTSS-T improves the localization accuracy mainly because the effect of outliers is reduced and lag induced by the target tracking Kalman filter is compensated for. RTSS-IT decreases the error even more because the images, from which the positions are estimated, are enhanced. In addition, RTSS-IT removes lag of the image filter which is significant

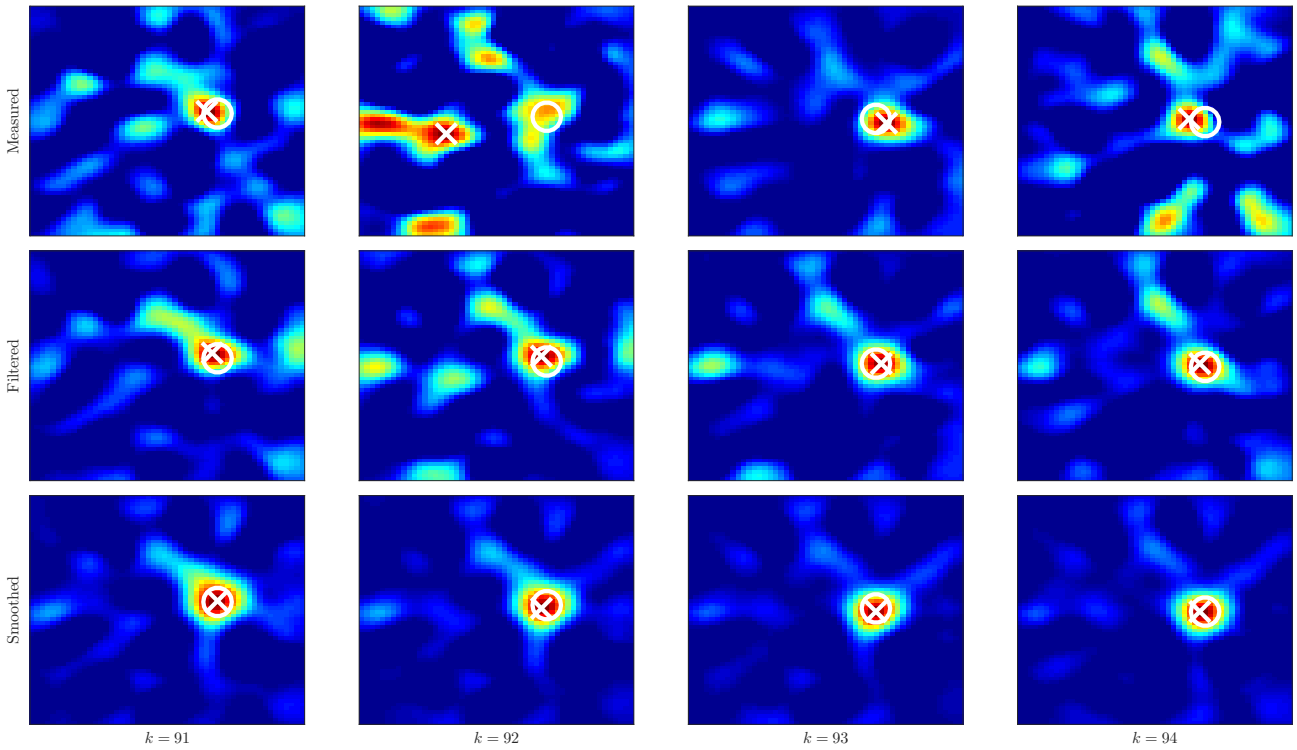

Fig. 6: The measured $\mathbf{z}_k^i$, filtered $\mathbf{x}_k^i$ and smoothed $\tilde{\mathbf{x}}_k^i$ propagation field images in Ex. 1. In the figures, the true position of the person is illustrated with a circle and the position estimate $\mathbf{z}_k^t$ using a cross

if the person is moving. Removing delay of the image filter is clearly visible in the open and through-wall experiments where the person is continuously in motion. TFS-IT results to the best accuracy. The algorithm not only removes the lag in image and position estimates, but it also improves the estimates of $w_{l,c}$ and $\mu_{l,c}$ in the backward recursion yielding better measurements $\mathbf{y}_k$ from which the images are created. This is especially important in challenging environments and when the experiment duration is relatively short as is the case in the through-wall experiment.

It can be concluded that in ideal environments ($\phi_{l,c} \ll 0$), channel diversity, the presented image filter and adaptive estimator do not improve the system performance significantly. The real benefits start to be visible as $\mu_\phi \to 0$ and there are links for which $\phi_{l,c} > 0$. In cluttered and challenging environments, such as the through-wall experiment, the importance of channel diversity increases and the system performance can be significantly improved by using the presented image filter and online estimator. Furthermore, the state estimates can always be improved using the presented smoothing filters.

VI. Experimental Validation

In this section, the development efforts are first quantitatively evaluated after which performance of the system is presented. Thereafter, model parameters $\phi_{l,c}$ and $\lambda_{l,c}$ for the different links and channels are estimated using data from the experiments. After the model parameters are estimated using batch-training, the system performance is re-evaluated. In this section, ARTI is evaluated with respect to *fade level RTI* (FLRTI). FLRTI weights the different channels based on their fade level and averages the measurements across the entire set of used channels, i.e., $y_l(k) = -\frac{1}{C}\sum_{c=1}^{C} \hat{w}_{l,c}\left(\tilde{r}_{l,c}(k) - \mu_{l,c}(k)\right)$, where $\hat{w}_{l,c}$ is the fade level based weight [4].

In Ex. $3-4$, $q^i = 0.1$ because in these experiments the number of used channels is four times greater than in Ex. $1-2$. Using a lower q^i value implies that the confidence in the model is increased and reactiveness to new measurements is decreased which is desirable when all 16 frequency channels are used.

A. Quantitative evaluation

The presented system comprises of three significant advancements to increase the accuracy and performance of state-of-the-art RTI systems. First, the images are filtered using a Kalman filter. This is beneficial because now the previous state of the propagation field $\mathbf{x}_{k-1}^i$ is taken into account. In past works, it is not considered how the person altered the propagation field at the previous time instant and valuable information is lost. The second benefit of the image filter is that the images can be enhanced using well known smoothing filters. The third advantage is that the system can be designed so that the delay in $\mathbf{x}_k^i$ is significantly lower than in systems that combine the RSS measurements on different channels by weighting and averaging [4], [8]. Averaging the channel measurements over the set of used channels inevitably introduces a delay in $\mathbf{z}_k^i$ which also effects $\mathbf{z}_k^t$. Length of this delay is determined by parameters of the system such as transmission interval of the

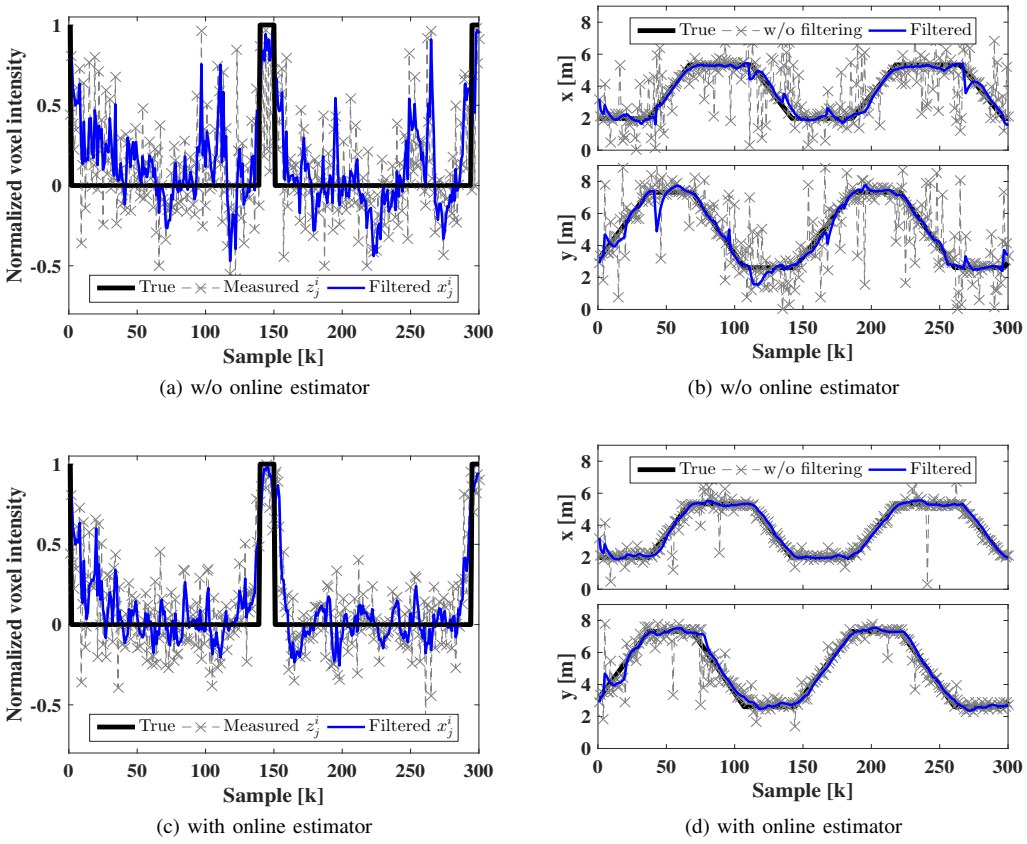

(a) w/o online estimator

(b) w/o online estimator

(c) with online estimator

(d) with online estimator

Fig. 7: In (a), the true, measured and filtered voxel intensity value without estimating $w_{l,c}$. In (b), the resulting coordinate estimates. In (c), $w_{l,c}$ is estimated recursively and in (d), the resulting coordinate estimates.

sensors, number of used sensors and channels, and velocity of the person.

Filtering the propagation field images is illustrated in Fig. 6. On the top row, propagation field images $\mathbf{z}_k^i$ at four successive TDMA cycles are shown. The position estimate $\mathbf{z}_{k=91}^t$ is accurate, but at the next time instant the estimate is poor because $\mathbf{z}_{k=92}^i$ does not capture the person's effect to the channel correctly. The filtered propagation field images $\mathbf{x}_k^i$ are illustrated on the middle row, and as shown, filtering improves quality of the images leading to an enhancement in localization accuracy. Essentially, the image filter suppresses noise of the low quality image stream and adapts to slowly varying changes caused by the target.

The second key contribution of the presented system is the recursive algorithm that is used for estimating the reference RSS value $\mu_{l,c}$ and expected direction of RSS change $w_{l,c}$. Estimating $\mu_{l,c}$ online is crucial for maintaining the system's ability to locate the target in the long run as propagation patterns of radio signals change [4], [3]. Respectively, correct estimation of $w_{l,c}$ enables the reconstruction of more accurate images with higher resolution.

The advantage of filtering and estimating $w_{l,c}$ online is illustrated in Fig. 7. The normalized intensity of a single voxel is shown in Fig. 7a. As illustrated, the measurements are very noisy resulting to extremely bad position estimates as shown in Fig. 7b. The image filter improves estimates of the individual voxels, enhances the image quality and reduces the positioning errors as depicted in the figures. Estimating $w_{l,c}$ recursively further improves the accuracy and resolution of $\mathbf{z}_k^i$ as illustrated in Fig. 7c. Together with the image filter, this leads to a considerable improvement in tracking accuracy as shown in Fig. 7d. It is to be noted that the measured voxel values are inaccurate in the beginning of the experiment $k < 50$ but the recursive algorithm is quickly capable of estimating $w_{l,c}$ correctly. Correspondingly, the coordinate estimates are inaccurate in the beginning of the experiment (approximately the same as w/o online learning) but already during the second lap, the estimated trajectory closely follows the true trajectory as illustrated in Fig. 7d.

The third contribution of the paper are the presented smoothing filters and batch-training. The smoothing filters presented in Section IV-D can be used to enhance the state estimates even further which might be beneficial in circumstances that do not require real-time estimates of the target state but demand as accurate estimates as possible. One such example is the presented batch-training algorithm which uses the smoothed state estimates $\tilde{\mathbf{x}}_k^t$ and mean-removed RSS $\mathbf{r}_k$ to estimate parameters of the system. Smoothing the images using the TF-based smoother is illustrated on the bottom row of Fig. 6. In general, the images and position estimates are more accurate when smoothing is applied.

TABLE V: Median (and 95$^{\text{th}}$ percentile) localization errors in centimeters

		Ex. 1	Ex. 2	Ex. 3	Ex. 4
ONLINE	flRTI	22.61 (51.21)	19.92 (149.71)	22.38 (79.45)	67.79 (220.49)
	ARTI w/o online est.	21.51 (99.81)	26.76 (140.83)	23.32 (104.64)	111.15 (297.92)
	ARTI	19.58 (48.44)	14.63 (57.26)	18.58 (61.90)	43.67 (236.94)
SMOOTHED	flRTI, RTSS-T	21.19 (38.51)	15.93 (133.80)	19.47 (68.21)	65.03 (169.47)
	ARTI, RTSS-T	15.18 (36.84)	13.25 (54.67)	15.09 (41.81)	32.97 (163.13)
	ARTI, RTSS-IT	9.66 (36.05)	12.85 (51.35)	14.04 (38.35)	26.28 (172.07)
	ARTI, TFS-IT	7.60 (29.01)	11.34 (44.85)	13.09 (30.71)	19.64 (71.80)
TRAINED	ARTI, RTSS-T	17.32 (34.50)	15.58 (50.43)	16.76 (37.80)	25.35 (125.33)
	ARTI, RTSS-IT	16.00 (32.63)	15.23 (49.13)	16.09 (37.50)	22.72 (72.83)
	ARTI, TFS-IT	13.66 (29.55)	14.67 (42.02)	15.68 (35.28)	19.03 (65.92)
	ARTI-online	16.70 (38.47)	14.67 (52.88)	16.19 (43.84)	31.63 (144.10)
	ARTI-true	13.41 (30.88)	12.44 (35.66)	10.94 (28.70)	20.57 (48.75)

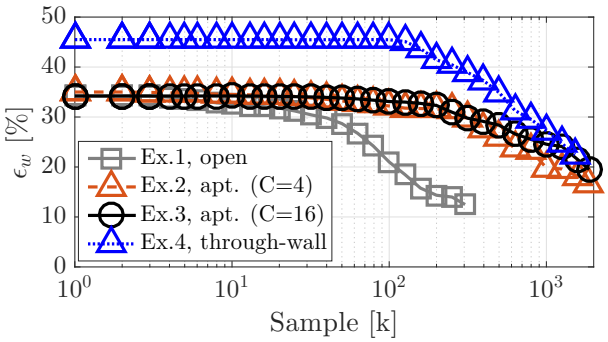

Fig. 8: Error of estimating $w_{l,c}$.

B. Experimental Results

The experimental results are given on rows $2-4$ of Table V. On average, FLRTI achieves high accuracy in experiments $1-3$. However, in Ex. 2, there are position estimates that are very inaccurate as indicated by the high 95$^{\text{th}}$ percentile value. Also, the performance in the through-wall experiment is satisfactory and the positioning error is considerably higher than in the other experiments. Comparing these results with the system that does not utilize the online estimator, one can see that the achieved accuracy of FLRTI is higher. This indicates that there is information in the steady-state RSS statistics that can be used to enhance the positioning accuracy. Therefore, the obtained results support the development efforts of earlier works that exploit channel diversity and fade level based weighting [8], [3], [4], [9].

As shown on fourth row of Table V, ARTI outperforms FLRTI in every experiment when the online estimator is enabled. The 95$^{\text{th}}$ percentile localization errors of ARTI are relatively high because in the beginning of the experiments the position estimates are poor as discussed in the previous subsection. However, the accuracy of ARTI improves considerably as more data is acquired and as the estimates of $w_{l,c}$ improve. The accuracy of estimating $w_{l,c}$ is illustrated in Fig. 8, where the true weight used in Eq. (25) is estimated using the batch-training algorithm and known trajectory of the person. As shown, the percentage error ϵ_w decreases as more measurements are acquired improving the accuracy of the state estimates.

Results of the different smoothing filters are given on rows $5-8$ of Table V and they are inline with the simulation results. Thus, the reader is referred to the discussion in Section V-C where the differences and benefits of the algorithms were presented.

C. Training the Model Parameters

In this subsection, the smoothed state estimates obtained in the previous subsection are used as input to the batch-training algorithm presented in Section IV-E. In addition, we consider a system that does not utilize batch-training and that solely uses the recursive estimate of $\phi_{l,c}$ obtained in the previous subsection. This training scheme is denoted as ARTI-online in Table V. For comparison, we also estimate $\phi_{l,c}$ and $\lambda_{l,c}$ using the person's known locations in order to study achievable accuracy of the system. This training scheme is denoted as ARTI-true in Table V. To avoid using the same data for training and validation, the experiments are re-conducted.

The online localization accuracy with the trained model parameters are given on rows $9-13$ of Table V and as can be seen, the accuracy of ARTI improves as a result of training. In general, the more accurate the position estimates used for training are, the better the localization accuracy is during online operation. Of the different training schemes, parameters trained with TFS-IT results to the best accuracy and it nearly achieves the same performance as the system that is trained with known trajectory of the person. Given the simulation and experimental results, it can be concluded that the presented system achieves high accuracy in every experiment and a significant improvement over FLRTI. Example trajectories of ARTI, TFS-IT in Ex. 3 and Ex. 4 are illustrated in Fig. 9.

D. Discussion

The computational overhead of the image filter and online estimator is small. On average, the execution time is 2.12 ms with FLRTI and 2.25 ms with ARTI in Ex. 1 using a Matlab implementation and a standard laptop equipped with a 2.70 GHz Intel Core i7-4800MQ processor and 16.0 GB of RAM memory. Since one TDMA cycle lasts 87 ms, online operation can be easily guaranteed. The execution time of the smoothing algorithms are 54 µs, 396 µs and 2380 µs per TDMA cycle for RTSS-T, RTSS-IT and TFS-IT algorithms in corresponding order. Thus, the higher performance of TFS-IT comes with the expense of increased computational overhead.

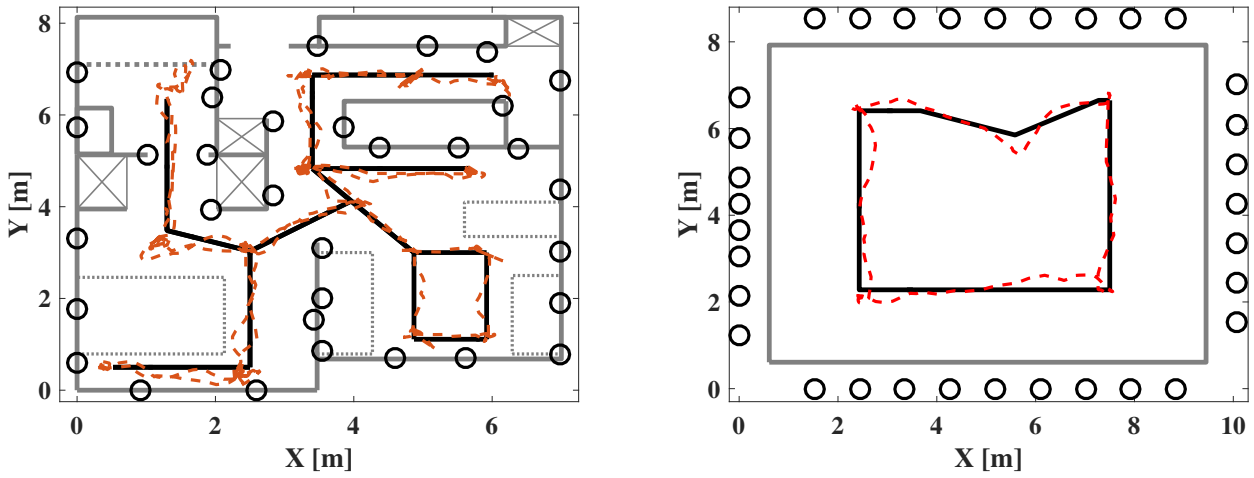

(a) apartment ($C = 16$) (b) through-wall

Fig. 9: Example trajectories of ARTI, TFS-IT. In the figures, the true trajectory is illustrated with the solid black line, the estimated with dashed red line and black circles indicate the sensor locations.

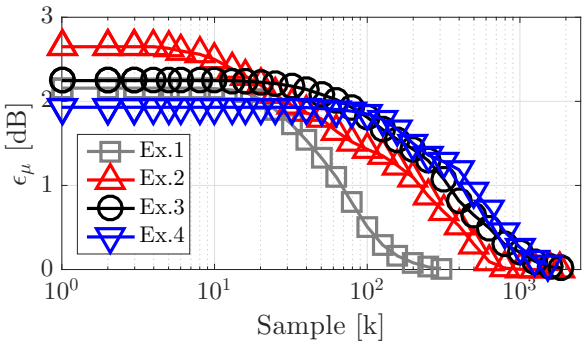

Fig. 10: Accuracy of estimating $\mu_{l,c}$ w/o a calibration period

The used training scheme should be selected based on requirements of the system. If it is necessary to achieve high localization accuracy as quickly as possible, then batch-training should be used. In this case, the simulation and experimental results support using TFS-IT. On the other hand, if the deployed system operates over an extended period of time, the benefit of batch-training diminishes. As depicted in Table V, ARTI-online already achieves comparative performance with respect to the batch-training systems, despite the fact that the conducted experiments were relatively short. Furthermore, this difference is expected to diminish even more over long periods of time when a rich set of RSS measurements are acquired.

The developed system is not required to have a calibration period before the person enters the monitored area. If the system is not calibrated, the first received RSS measurement is used as the reference RSS value. This will result into the situation where the state estimates are inaccurate in the beginning of the experiment. However, after the person starts to move, the person can be correctly localized because the reference values, for links that were initially far away from the person, are close to the real reference values. Let us denote the reference value at time k without the calibration period as $\mu_{l,c}^{w/o}(k)$ and with the calibration period as $\mu_{l,c}(k)$. The root mean squared error is calculated as

$$\epsilon_\mu(k) = \sqrt{\frac{1}{L \cdot C} \sum_{l=1}^{L} \sum_{c=1}^{C} \left(\mu_{l,c}(k) - \mu_{l,c}^{w/o}(k) \right)^2}$$

and illustrated in Fig. 10. As shown, $\mu_{l,c}^{w/o}$ converges to $\mu_{l,c}$ as more measurements are gathered. Thus, long-term deployments are not required to have a calibration period if the subject is moving and the loss of accuracy is acceptable in the beginning of the experiment.

Typically, RF tomography systems achieve high localization accuracy with the expense of deploying numerous sensors in the monitored area. For example, the sensor density in the experiments ranges from 0.57 sensors/m2 in Ex. 2 and Ex. 3 to 0.38 sensors/m2 in Ex. 4. On average, resolution of the images degrades and the localization error increases when the sensor number is decreased as demonstrated for example in [3], [9]. However, with fewer sensors the sampling rate for each link respectively increases improving the tracking accuracy and the convergence rate of the online estimator. On the other hand, the number of used communication channels could be increased without decreasing the sampling frequency which in turn is expected to improve the localization accuracy. Thus, it is not a straightforward task to evaluate how much the accuracy degrades when fewer sensors are used. Simulating node removal, the median tracking error is doubled when third of the sensors are randomly removed from the different experiments and in the best case, the localization accuracy remains the same. The results imply that the remaining nodes should be evenly distributed to assure accurate localization throughout the monitored area.

VII. Conclusions

This paper presents ARTI, an adaptive radio tomographic imaging system. Novelty of the system are in its adaptive measurement unit and in the image filter. Online estimation of the model parameters enables the system to adapt to the intrinsic nature of the different links, channels and environment. On the other hand, the image filter makes it possible to take into account temporal changes of the propagation field. The paper also presents different smoothing filters and batch-training is explored to estimate unknown parameters of the system. The results demonstrate that ARTI achieves high accuracy in three different environments, the state estimates can be enhanced using smoothing, and improved localization accuracy can be achieved using batch-training.

To date, research on RF tomography has mainly concentrated on deriving more accurate spatial models since they dictate the achievable accuracy of these systems. However, we have demonstrated in this paper that high accuracy tracking can be achieved using a coarse RSS model and by estimating its parameters online. Generally speaking, this paper scratches the surface of online parameter estimation and the paper is to motivate the readers toward this area of research. The used EWMA estimators are simplistic and more advanced options are available and subjects of future research. Future research should answer at least the following questions. Is it possible to use for example the model in Eq. (9) and estimate its parameters using an extended Kalman filter or some other non-linear filter? What about more sophisticated RSS models, can we estimate their parameters? If the parameter estimates diverge, is it possible to identify these occurrences and recover from them?

Acknowledgments

This work is funded by Doctoral Programme in Electrical Engineering at Aalto University. This material is also based upon the work supported by Academy of Finland, under project number 299099.

References

[1] K. Woyach, D. Puccinelli, and M. Haenggi, "Sensorless sensing in wireless networks: Implementation and measurements," in *Modeling and Optimization in Mobile, Ad Hoc and Wireless Networks, 2006 4th International Symposium on*, April 2006, pp. 1–8.

[2] N. Patwari and J. Wilson, "Rf sensor networks for device-free localization: Measurements, models, and algorithms," *Proceedings of the IEEE*, vol. 98, no. 11, pp. 1961–1973, Nov 2010.

[3] O. Kaltiokallio, M. Bocca, and N. Patwari, "Follow @grandma: Long-term device-free localization for residential monitoring," in *Local Computer Networks Workshops (LCN Workshops), 2012 IEEE 37th Conference on*, Oct 2012, pp. 991–998.

[4] M. Bocca, O. Kaltiokallio, and N. Patwari, "Radio tomographic imaging for ambient assisted living," in *Evaluating AAL Systems Through Competitive Benchmarking*, ser. Communications in Computer and Information Science, S. Chessa and S. Knauth, Eds. Springer Berlin Heidelberg, 2013, vol. 362, pp. 108–130.

[5] M. Björkbom, J. Timonen, H. Yigitler, O. Kaltiokallio, J. M. V. Garcia, M. Myrsky, J. Saarinen, M. Korkalainen, C. Cuhac, R. Jäntti, R. Virrankoski, J. Vankka, and H. N. Koivo, "Localization services for online common operational picture and situation awareness," *IEEE Access*, vol. 1, pp. 742–757, 2013.

[6] J. Wilson and N. Patwari, "A fade-level skew-laplace signal strength model for device-free localization with wireless networks," *IEEE Transactions on Mobile Computing*, vol. 11, no. 6, pp. 947–958, June 2012.

[7] Y. Zheng and A. Men, "Through-wall tracking with radio tomography networks using foreground detection," in *2012 IEEE Wireless Communications and Networking Conference (WCNC)*, April 2012, pp. 3278–3283.

[8] O. Kaltiokallio, M. Bocca, and N. Patwari, "Enhancing the accuracy of radio tomographic imaging using channel diversity," in *Mobile Adhoc and Sensor Systems (MASS), 2012 IEEE 9th International Conference on*, Oct 2012, pp. 254–262.

[9] ——, "A fade level-based spatial model for radio tomographic imaging," *IEEE Transactions on Mobile Computing*, vol. 13, no. 6, pp. 1159–1172, June 2014.

[10] M. Youssef, M. Mah, and A. Agrawala, "Challenges: Device-free passive localization for wireless environments," in *Proceedings of the 13th Annual ACM International Conference on Mobile Computing and Networking*, 2007, pp. 222–229.

[11] C. Xu, B. Firner, R. S. Moore, Y. Zhang, W. Trappe, R. Howard, F. Zhang, and N. An, "Scpl: Indoor device-free multi-subject counting and localization using radio signal strength," in *Information Processing in Sensor Networks (IPSN), 2013 ACM/IEEE International Conference on*, April 2013, pp. 79–90.

[12] B. Mager, P. Lundrigan, and N. Patwari, "Fingerprint-based device-free localization performance in changing environments," *IEEE Journal on Selected Areas in Communications*, vol. 33, no. 11, pp. 2429–2438, Nov 2015.

[13] N. Patwari and P. Agrawal, "Effects of correlated shadowing: Connectivity, localization, and rf tomography," in *Information Processing in Sensor Networks, 2008. IPSN '08. International Conference on*, April 2008, pp. 82–93.

[14] J. Wilson and N. Patwari, "Radio tomographic imaging with wireless networks," *IEEE Transactions on Mobile Computing*, vol. 9, no. 5, pp. 621–632, May 2010.

[15] S. Savazzi, M. Nicoli, F. Carminati, and M. Riva, "A bayesian approach to device-free localization: Modeling and experimental assessment," *IEEE Journal of Selected Topics in Signal Processing*, vol. 8, no. 1, pp. 16–29, Feb 2014.

[16] Z. Wang, H. Liu, S. Xu, X. Bu, and J. An, "A diffraction measurement model and particle filter tracking method for rss-based dfl," *IEEE Journal on Selected Areas in Communications*, vol. 33, no. 11, pp. 2391–2403, Nov 2015.

[17] Y. Li, X. Chen, M. Coates, and B. Yang, "Sequential monte carlo radio-frequency tomographic tracking," in *Acoustics, Speech and Signal Processing (ICASSP), 2011 IEEE International Conference on*, May 2011, pp. 3976–3979.

[18] J. Wilson and N. Patwari, "See-through walls: Motion tracking using variance-based radio tomography networks," *IEEE Transactions on Mobile Computing*, vol. 10, no. 5, pp. 612–621, May 2011.

[19] Y. Zhao, N. Patwari, J. M. Phillips, and S. Venkatasubramanian, "Radio tomographic imaging and tracking of stationary and moving people via kernel distance," in *Proceedings of the 12th International Conference on Information Processing in Sensor Networks*, 2013, pp. 229–240.

[20] D. Maas, J. Wilson, and N. Patwari, "Toward a rapidly deployable radio tomographic imaging system for tactical operations," in *Local Computer Networks Workshops (LCN Workshops), 2013 IEEE 38th Conference on*, Oct 2013, pp. 203–210.

[21] Y. Zhao and N. Patwari, "Robust estimators for variance-based device-free localization and tracking," *IEEE Transactions on Mobile Computing*, vol. 14, no. 10, pp. 2116–2129, Oct 2015.

[22] S. Nannuru, Y. Li, Y. Zeng, M. Coates, and B. Yang, "Radio-frequency tomography for passive indoor multitarget tracking," *IEEE Transactions on Mobile Computing*, vol. 12, no. 12, pp. 2322–2333, Dec 2013.

[23] Y. Guo, K. Huang, N. Jiang, X. Guo, Y. Li, and G. Wang, "An exponential-rayleigh model for rss-based device-free localization and tracking," *IEEE Transactions on Mobile Computing*, vol. 14, no. 3, pp. 484–494, March 2015.

[24] O. Kaltiokallio, H. Yigitler, and R. Jäntti, "A three-state received signal strength model for device-free localization," *CoRR*, vol. abs/1402.7019, 2014. [Online]. Available: http://arxiv.org/abs/1402.7019

[25] A. Edelstein and M. Rabbat, "Background subtraction for online calibration of baseline rss in rf sensing networks," *IEEE Transactions on Mobile Computing*, vol. 12, no. 12, pp. 2386–2398, Dec 2013.

[26] R. K. Martin, A. Folkerts, and T. Heinl, "Accuracy vs. resolution in radio tomography," *IEEE Transactions on Signal Processing*, vol. 62, no. 10, pp. 2480–2491, May 2014.

[27] H. Yiitler and R. Jntti, "Experimental accuracy assessment of radio tomographic imaging methods," in *2016 IEEE International Conference on Pervasive Computing and Communication Workshops (PerCom Workshops)*, March 2016, pp. 1–6.

[28] N. Patwari, L. Brewer, Q. Tate, O. Kaltiokallio, and M. Bocca, "Breathfinding: A wireless network that monitors and locates breathing in a home," *IEEE Journal of Selected Topics in Signal Processing*, vol. 8, no. 1, pp. 30–42, Feb 2014.
[29] J. Wilson, N. Patwari, and O. G. Vasquez, "Regularization methods for radio tomographic imaging," in *in 2009 Virginia Tech Symposium on Wireless Personal Communications*, 2009.
[30] M. Bocca, O. Kaltiokallio, N. Patwari, and S. Venkatasubramanian, "Multiple target tracking with rf sensor networks," *IEEE Transactions on Mobile Computing*, vol. 13, no. 8, pp. 1787–1800, Aug 2014.
[31] Q. Wang, H. Yigitler, R. Jäntti, and X. Huang, "Localizing multiple objects using radio tomographic imaging technology," *IEEE Transactions on Vehicular Technology*, vol. PP, no. 99, pp. 1–1, 2015.
[32] Y. Bar-Shalom and X.-R. Li, *Estimation with Applications to Tracking and Navigation*. New York, NY, USA: John Wiley & Sons, Inc., 2001.
[33] S. Särkkä, *Bayesian Filtering and Smoothing*. Cambridge University Press, 2013.
[34] D. Fraser and J. Potter, "The optimum linear smoother as a combination of two optimum linear filters," *IEEE Transactions on Automatic Control*, vol. 14, no. 4, pp. 387–390, Aug 1969.
[35] J. C. Lagarias, J. A. Reeds, M. H. Wright, and P. E. Wright, "Convergence properties of the nelder–mead simplex method in low dimensions," *SIAM Journal on Optimization*, vol. 9, no. 1, pp. 112–147, 1998.
[36] Texas Instruments. A USB-enabled system-on-chip solution for 2.4 GHz IEEE 802.15.4 and ZigBee applications. [Online]. Available: http://www.ti.com/lit/ds/symlink/cc2531.pdf
[37] IEEE 802.15.4 standard technical specs. [Online]. Available: http://www.ieee802.org/15/pub/TG4Expert.html
[38] K. Srinivasan, P. Dutta, A. Tavakoli, and P. Levis, "Understanding the causes of packet delivery success and failure in dense wireless sensor networks," in *Proceedings of the 4th international conference on Embedded networked sensor systems (SenSys '06)*, 2006, pp. 419–420.

Ossi Kaltiokallio received the B.Sc. and M.Sc. degrees in electrical engineering from the School of Electrical Engineering, Aalto University, Helsinki, Finland, both in 2011. He is currently a Ph.D. student with the department of Communications and Networking at Aalto University School of Electrical Engineering where he holds an ELEC doctoral school position as of January 2014. He is the recipient of SenseApp 2012 and IPSN 2014 conference best paper awards. His current research interests include RF propagation, RSS-based localization and tracking, signal processing and Bayesian inference.

Riku Jäntti (M'02 - SM'07) is an Associate Professor (tenured) in Communications Engineering and the head of the department of Communications and Networking at Aalto University School of Electrical Engineering, Finland. He received his M.Sc (with distinction) in Electrical Engineering in 1997 and D.Sc (with distinction) in Automation and Systems Technology in 2001, both from Helsinki University of Technology (TKK). Prior to joining Aalto (formerly known as TKK) in August 2006, he was professor pro tem at the Department of Computer Science, University of Vaasa. Prof. Jäntti is a senior member of IEEE and associate editor of IEEE Transactions on Vehicular Technology. He is also IEEE VTS Distinguished Lecturer (Class 2016). The research interests of Prof. Jäntti include radio resource control and optimization for machine type communications, Cloud based Radio Access Networks, spectrum and co-existence management and RF Inference.

Neal Patwari received the B.S. (1997) and M.S. (1999) degrees from Virginia Tech, and the Ph.D. from the University of Michigan, Ann Arbor (2005), all in Electrical Engineering. He was a research engineer at Motorola Labs, Florida, between 1999 and 2001. He is an Associate Professor in the Department of Electrical and Computer Engineering at the University of Utah. He directs the Sensing and Processing Across Networks (SPAN) Lab, which performs research at the intersection of statistical signal processing and wireless networking. Neal is also the Director of Research at Xandem Technology. He has received best paper awards from the IEEE Signal Processing Magazine (2009), SenseApp (2012), and IPSN (2014), and the 2011 University of Utah Early Career Teaching Award.